Physical Constraints from Near-infrared Fast Photometry of the Black Hole Transient GX 339–4

F. M. Vincentelli[1] , P. Casella[2] , P. Petrucci[3] , T. Maccarone[4] , D. M. Russell[5] , P. Uttley[6], B. De Marco[7] , R. Fender[8], P. Gandhi[1] , J. Malzac[9] , K. O'Brien[10] , and J. A. Tomsick[11]

[1] Department of Physics and Astronomy, University of Southampton, Southampton SO17 1BJ, UK; F.M.Vincentelli@soton.ac.uk
[2] INAF, Osservatorio Astronomico di Roma Via Frascati 33, I-00078 Monteporzio Catone, Italy
[3] Univ. Grenoble Alpes, CNRS, IPAG, F-38000 Grenoble, France
[4] Texas Tech University, Physics & Astronomy Department, Box 41051, Lubbock, TX 79409-1051, USA
[5] Center for Astro, Particle and Planetary Physics, New York University Abu Dhabi, P.O. Box 129188, Abu Dhabi, UAE
[6] Astronomical Institute, Anton Pannekoek, University of Amsterdam, Science Park 904, NL-1098 XH Amsterdam, The Netherlands
[7] Nicolaus Copernicus Astronomical Center, Polish Academy of Sciences, Bartycka 18, PL-00-716 Warsaw, Poland
[8] Department of Physics, Astrophysics, University of Oxford, Denys Wilkinson Building, Keble Road, Oxford OX1 3RH, UK
[9] IRAP, Université de Toulouse, CNRS, UPS, CNES, Toulouse, France
[10] Department of Physics, Durham University, South Road, Durham DH1 3LE, UK
[11] Space Sciences Laboratory, 7 Gauss Way, University of California, Berkeley, CA 94720, USA

Abstract

We present results from the first multi-epoch X-ray/IR fast-photometry campaign on the black hole transient GX 339–4, during its 2015 outburst decay. We studied the evolution of the power spectral densities finding strong differences between the two bands. The X-ray power spectral density follows standard patterns of evolution, plausibly reflecting changes in the accretion flow. The IR power spectral density instead evolves very slowly, with a high-frequency break consistent with remaining constant at 0.63 ± 0.03 Hz throughout the campaign. We discuss this result in the context of the currently available models for the IR emission in black hole transients. While all models will need to be tested quantitatively against this unexpected constraint, we show that an IR-emitting relativistic jet that filters out the short-timescale fluctuations injected from the accretion inflow appears as the most plausible scenario.

Unified Astronomy Thesaurus concepts: Stellar accretion disks (1579); Jets (870); Black hole physics (159); Low-mass X-ray binary stars (939)

1. Introduction

Black hole X-ray binaries (BHXRBs) are systems in which a stellar-mass black hole has a companion star in close orbit, leading to the transfer of mass from the star to the hole. They are strong multiwavelength emitters, showing a complex and variable spectrum from radio frequencies to hard X-rays (see, e.g., Fender et al. 2000; Markoff et al. 2001; Corbel & Fender 2002; Gandhi et al. 2011; Corbel et al. 2013 and references therein). The time-averaged spectrum is the result of variable broadband emission from a number of physical components, each emitting over broad and overlapping energy ranges. In their so-called "hard states," the X-ray spectra of BHXRBs are dominated by a power-law component, with a cutoff at around 100 keV (Motta et al. 2009; Kalemci et al. 2014), which is generally believed to arise from an optically thin, geometrically thick inflow (Thorne & Price 1975; Narayan & Yi 1995; Zdziarski & Gierliński 2004; Done et al. 2007). This hot plasma Comptonizes thermal, colder (ultraviolet to soft X-rays) photons from an accretion disk and perhaps also less energetic (optical or even infrared) synchrotron photons from the inflow itself (Malzac & Belmont 2009; Poutanen & Vurm 2009; Veledina et al. 2011, 2013). At longer wavelengths, a flat (or slightly inverted) spectrum from radio down to optical-to-infrared (O-IR) can be seen, representing clear evidence for the presence of a compact jet (Corbel & Fender 2002; Gandhi et al. 2011; Russell et al. 2016). Consensus has not been reached yet on the quantitative contribution of each of these spectral components at different wavelengths, nor on their evolution.

Studies of the fast variability properties of the X-ray emission have been historically very important—albeit inconclusive—to constrain physical models (Nowak et al. 1999; Churazov et al. 2001; Ingram et al. 2009). The X-ray Fourier power spectral densities (PSDs) during the hard state reveal a combination of broadband components and narrow quasi-periodic oscillations (QPOs). The behavior of these components is closely related to the spectral evolution of these sources, with most of their characteristic frequencies increasing with the accretion rate and/or with the softening of the X-ray emission (Belloni et al. 2002, 2005). The characteristic frequencies of the X-ray broadband noise are often associated with the viscous timescales at some radii in the accretion flow, so that their evolution is explained in terms of a geometrical evolution of the accretion flow, which is thought to become more and more compact while the source evolves from a hard to soft spectral state. This interpretation is supported by the fact that the highest of these frequencies (the so-called "high-frequency break" in the X-ray PSD) appears to saturate at a few Hz (Churazov et al. 2001; Belloni et al. 2005; Ingram & Done 2012): a value consistent with the viscous timescale for a hot optically thin, geometrically thick inflow, at its innermost stable orbit around a stellar-mass black hole (Done et al. 2007). Further refinements of this broad picture came from more advanced X-ray spectral-timing techniques, where delays are studied as a function of both Fourier frequency and energy (see, e.g., Nowak et al. 1999; Kotov et al. 2001; Uttley et al. 2014; De Marco et al. 2017; Kara et al. 2019; Mahmoud et al. 2019 and references therein).

An alternative interpretation for the broadband components observed in the X-ray PSD has been recently suggested by Veledina (2016) in terms of interference between two Comptonization continua. Both these components would respond to the fluctuations of the mass accretion rate, but with a variable delay between them due to the evolving propagation timescale from the disk Comptonization radius to the synchrotron Comptonization region.

Strong rapid variability has been also observed at longer, O-IR wavelengths (Motch et al. 1982; Gandhi et al. 2008; Casella et al. 2010; Gandhi et al. 2016). The observed phenomenology is rather complex, with almost all the above-mentioned spectral components potentially contributing to the measured variability: thermally reprocessed emission from the outer disk, and synchrotron emission from the jet and from a magnetized inflow. In some cases, an inflow could reproduce neatly the data (Veledina et al. 2017), while in other cases a jet origin has been securely identified, at least for the fastest (subsecond) variability component (Gandhi et al. 2008) and especially at infrared wavelengths (Casella et al. 2010), often showing a ~ 0.1 s delay with respect to the X-ray variability. In at least some cases, an internal-shock jet model could reproduce successfully both the short-timescale variability and the average broadband spectral energy distribution (Malzac 2014; Malzac et al. 2018). Further data sets have yielded further constraints on the geometry of relativistic jets (Gandhi et al. 2017), and on the physical processes taking place at their base (Vincentelli et al. 2018).

Altogether, the study of the multiwavelength fast variability from BHXRBs has developed rapidly over the last years, showing a large potential for studying the physics of the accretion–ejection processes. Most of the results mentioned above were obtained with single observations, done on different sources or during different outbursts, which hampered investigations on the evolution of the various components. In this work we present results from a 1 month long monitoring campaign of the X-ray and IR fast variability properties of GX 339–4 during the decay of its 2015 outburst. During this phase, BHXRBs show a re-brightening in radio followed by an increase in luminosity at O-IR wavelengths (Corbel et al. 2013).

2. Observations

The campaign consisted of five quasi-simultaneous X-ray and IR observations spanning between 2015 September 2 (MJD 57267) and 2015 October 3 (MJD 57298). The X-ray observations were carried out with *XMM-Newton* (PI: Petrucci), while the IR data were collected with HAWK-I@VLT (Program ID 095.D-0211(A), PI: Casella). The full X-ray data set already has been described in detail by De Marco et al. (2017), who analyzed the evolution of the reverberation lag; by Stiele & Kong (2017), who reported timing and spectral analysis; and by Wang-Ji et al. (2018), who focused on the spectral properties. For an overview of the whole X-ray data set we refer the reader to these works. Here we focus on the properties of the IR variability and its comparison with the X-ray variability.

2.1. X-Ray Observations

We extracted data from the *XMM-Newton* Epic-pn camera (Strüder et al. 2001). The first three observations (2015 September 2, 7, and 12) were taken in *Timing* mode, while the last two (2015 September 17 and 30) in *Small window mode*. Following the procedure described in De Marco et al. (2017), we extracted the events in the 2–10 keV band, in a box of $\approx 86''$ of angular size in the first case (RAWX between 28 and 48), and within a circle of $40''$ around the source in the latter. The extracted curves were barycentered to the Barycentric Dynamical Time system, using the command *barycen*. All X-ray light curves were extracted with the highest time resolution available: i.e., 5.7 ms for the first three observations and 7.8 ms for the last two.

2.2. IR Data

We collected IR (K_s-band) high time resolution data with HAWK-I mounted at VLT UT-4/Yepun. HAWK-I is a near-infrared wide-field imager (0.97–2.31 μm) made by four HAWAII 2RG 2048 $\times$ 2048 pixel detectors (Pirard et al. 2004). In order to reach subsecond time resolution, the observations were performed in *Fast-Phot* mode, reading only a stripe made of 16 contiguous windows of 128 $\times$ 64 pixels in each quadrant. This allowed us to reach a time resolution as short as 0.105 s in the first two epochs (2015 September 6 and 7), 0.125 s for the third and fourth (2015 September 17 and 22), and 0.25 s for the last epoch (2015 October 3). The data have a short (≈ 3 s long) gap every 250 exposures, to empty the instrument buffer. Gaps where then filled using the method described in Kalamkar et al. (2016). The instrument was pointed as to place the target and a bright reference star ($K_s = 9.5$) in the lower left quadrant (Q1). Photometric data were extracted using the ULTRACAM data reduction software tools[12] (Dhillon et al. 2007). Parameters for the extraction were derived from the bright reference star and position, to which the position of the target was linked in each exposure. To account for seeing effects, the ratio between the source and the reference star count rate was used. The time of each frame was then put in the Barycentric Dynamical Time system.

3. Analysis and Results

The spectral analysis of the X-ray observation (reported by De Marco et al. 2017) showed that the source had already reached the hard state during our campaign. The average IR magnitude and X-ray count rate for each epoch are plotted in Figure 1, showing that we caught the source in its typical O-IR re-brightening (Dinçer et al. 2012; Corbel et al. 2013), with a peak on 2015 September 17.

In order to quantify the variability in the X-ray and IR bands, we computed the fast Fourier transform of both light curves for all the observations. For the X-rays we chose 65,536 bins per segment; for IR instead, we used 256 bins per segment for the first epoch and 1024 for remaining ones, due to the structure of the data. We then calculated the PSDs, adopting a fractional squared rms normalization (Belloni & Hasinger 1990). In Figure 2 (upper and middle panels) we plot the X-ray and IR PSDs from 2015 September 17. All the X-ray and IR PSDs revealed the broadband noise usually observed in the hard (-intermediate) state of BHXRBs (Belloni et al. 2005; Done et al. 2007). In order to measure any possible frequency-dependent lag between the two bands, we calculated the time lags between the two bands for the only epoch where there was

---

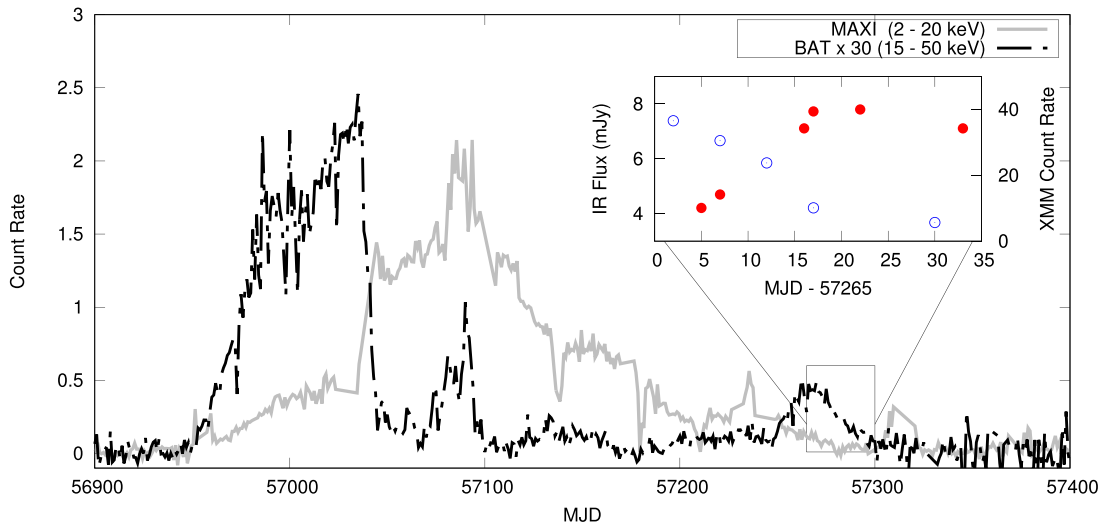12 See also http://deneb.astro.warwick.ac.uk/phsaap/ultracam/.

Figure 1. Long-term light curve measured by MAXI (gray solid curve) and *Swift* BAT (black dashed–dotted curve). The inset shows the evolution of the IR flux (red full points) and the 3–10 keV X-ray count rate measured by XMM (blue empty points) as a function of time during our campaign. The reference date for the light curve in the inset is 2015 August 31.

exact simultaneity, 2015 September 17, following the recipes described in Uttley et al. (2014). We report the time lag in the lower panel of Figure 2, where positive lags imply IR lagging the X-rays. At low frequencies the IR leads the X-rays by up to several seconds, while at high frequencies the IR lags the X-rays by ∼0.1 s. In the frequency ranges where the lags are detected the intrinsic coherence was found to be ≈0.2 (F. M. Vincentelli et al. 2019, in preparation).

Following Belloni et al. (2002, 2005) we modeled all the PSDs with a number of Lorentzian functions (PSD$(\nu) = \frac{r^2 \Delta}{2\pi}\big/[(\nu - \nu_0)^2 + (\Delta/2)^2])$. Three broad components were needed to approximate the X-ray broadband noise and we will refer to them hereafter respectively as $\nu_{X_{LF}}, \nu_{X_{IF}}$, and $\nu_{X_{HF}}$. One X-ray PSD (from the 2015 September 17 epoch) also showed marginal evidence for a narrower feature at 0.11 ± 0.01 Hz, which we identify as a type-C QPO (Casella et al. 2005; Motta et al. 2011). Two broad components (a low- and a high-frequency one, $\nu_{IR_{LF}}$ and $\nu_{IR_{HF}}$) were instead found to be sufficient to approximate the IR broadband noise. However, in all the IR PSDs but the last one, an additional Lorentzian component (hereafter $\nu_{IR_{QPO}}$) was needed to account for the presence of a narrow feature. We identify this narrow component as a type-C QPO, as its frequency on 2015 September 17 is consistent with the one of the simultaneous X-ray type-C QPOs.

In Figure 3 we show the time evolution of the characteristic frequencies ($\nu_{char} = \sqrt{\nu_0^2 + (\Delta/2)^2}$) of all the components. Linear fits as a function of time ($\nu = -a\,t + b$) are reported in Table 1. We note that the slope of the high-frequency IR component is consistent with zero: we therefore also fitted this component with a constant, obtaining $\nu_{IR_{HF}} = 0.63 \pm 0.03$ Hz. We also performed linear fits ($\nu_1 = a\,\nu_2 + b$) to quantify possible correlations between the low- and high-frequency components (see Table 1). We could not perform direct fits to quantify possible correlations between X-ray and IR frequencies, as most of the measurements are not simultaneous. However, by linking the fits of their individual time evolution we find that the low-frequency IR component $\nu_{IR_{LF}}$ is consistent with having a constant offset of ∼0.05 Hz with respect to the

X-ray low-frequency component $\nu_{X_{LF}}$ (see the inset in Figure 3).

The large uncertainties and the small number of points do not allow us to perform useful statistical tests on these correlations. This is particularly true for $\nu_{IR_{HF}}$, which is consistent with either being constant or with having a constant offset with respect to a slowly declining $\nu_{IR_{LF}}$.

4. Discussion

We have discovered a peculiar evolution of the characteristic frequencies of the IR emission from the BHT GX 339–4, during its 2015 outburst decay. Namely, while the X-ray PSD shows the expected behavior, with all its characteristic frequencies remaining proportional to each other (i.e., with a constant ratio) while decreasing by about a factor of 5 in about 30 days, the IR PSD reveals a relatively stable broadband noise, with its characteristic frequencies decaying only very slowly. The IR low-frequency component is consistent with following closely the X-ray low-frequency one, with a constant offset of ∼0.05 Hz (see the inset in Figure 3). The type-C QPO evolves more rapidly, with a decaying rate relatively similar to that of the X-ray intermediate-frequency component. What is surprising is the slow decay of the IR high-frequency component, which appears clearly disconnected from the X-ray high-frequency component. Instead, it is consistent with having a constant offset of ∼0.54 Hz with respect to the IR low-frequency component, as well as with being approximately unchanging at ∼0.63 Hz throughout the campaign.

The detection of such a distinctive evolution of the IR PSD holds a strong interpretative potential, as it provides constraints to the main models discussed in the literature for the IR emission from BHTs: reprocessing from the outer disk, synchrotron emission from a magnetized inflow, and synchro-tron emission from a jet. An IR low-frequency component correlated with the X-ray low-frequency one is perhaps naturally accounted for in all scenarios. The substantial stability of the IR high-frequency component is instead more constraining. The statistics of the data do not allow us to conclude whether this component is decaying very slowly or constant, but in either case it is clear that its evolution is disconnected
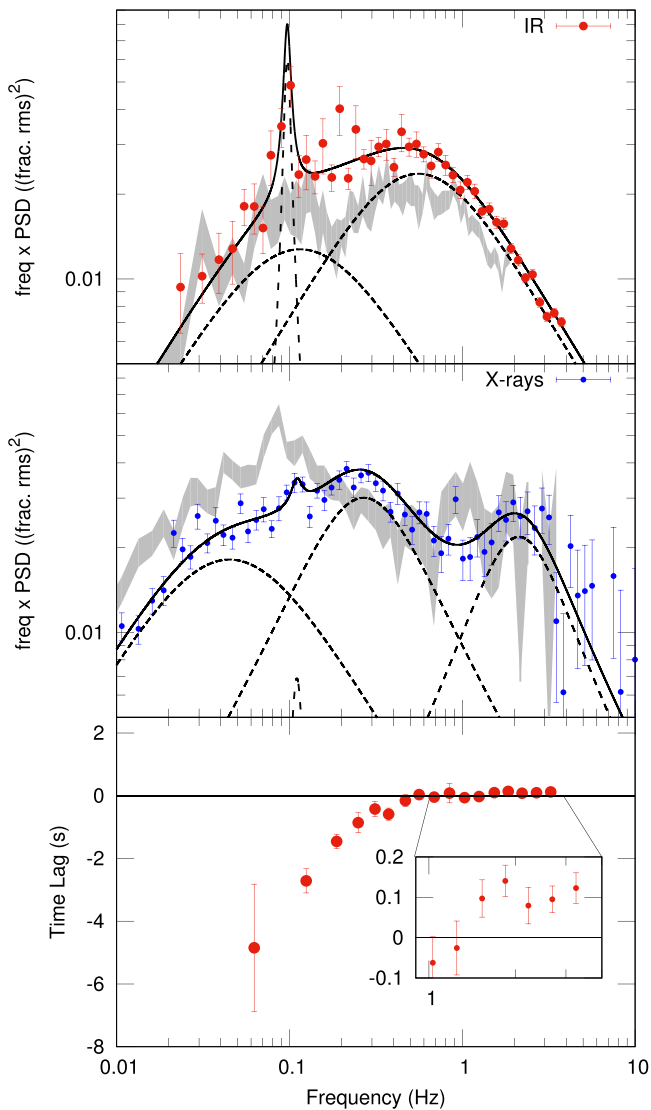
Figure 2. Results from the Fourier analysis of the strictly simultaneous observation on 2015 September 17. Top panels: PSDs computed with 1024 (IR) and 16384 (X-ray) bins per segments. The dotted lines indicate the Lorentzian components used to model the PSDs. The gray curves represent the PSDs measured on the last epochs of the campaign, namely, on 2015 October 3 (X-rays) and September 30 (IR), for comparison. Bottom panel: frequency-dependent time lags, computed with 128 bins per segment. Positive lags imply IR lagging the X-rays.

from that of the X-ray high-frequency component. At the same time, the time lags show that the variability in the two bands is correlated over a broad range of frequencies, including those above the IR high-frequency break (Figure 2), which implies the two signals are not independent.

We note that, so far, all the reported fast-photometry O-IR observations of GX 339-4 have revealed a high-frequency component at similar frequencies as reported here, although never in the same outburst (Casella et al. 2010; Gandhi et al. 2010; Kalamkar et al. 2016; Vincentelli et al. 2018). This might suggest that this frequency is indeed constant, but further observations, especially longer monitoring campaigns, will be needed to confirm this.

In the following, we discuss the implications of these results in the context of possible physical scenarios.

4.1. Outer Disk

The observed stability of the IR high-frequency component could be easily explained if the observed IR variability were dominated by reprocessing of the X-ray emission from the outer disk. The maximum IR frequency would be then related to the disk response function, which is not expected to change with time.

However, the lags we measure are too small to be consistent with the travel time from the X-ray-emitting inner regions of the flow to the IR-emitting outer regions of the disk (or even negative; see Figure 2, lower panel). Additionally, the same 0.1 s delay has been already reported a few times for this source, and in those cases a thermal origin (Gandhi et al. 2008, 2017; Casella et al. 2010) had been robustly excluded. Thus, we conclude that the reprocessing scenario can be securely discarded.

4.2. Hot Inflow

We consider here the hypothesis that the whole IR variable emission comes from a magnetized inflow, and that the evolution of the X-ray PSD is interpreted in terms of interference between two Comptonization continua (Veledina et al. 2013; Veledina 2016). The observed IR variable emission would then correspond to the seed synchrotron photons emitted before the Comptonization takes place in the hot inflow, and therefore can be interpreted as a proxy for the mass accretion rate. A slow decay of all the IR characteristic frequencies could then be associated with a slowly evolving geometry of the accretion inflow (Ingram & Done 2012; Ingram et al. 2016). To maintain a constant O-IR high-frequency component within this scenario would require that the magnetized inflow extends beyond ≈50 Schwarzschild radii (or 100 gravitational radii, $R_G = GM/c^2$) during the entire re-brightening phase. Most of the IR flux as well as variability in the magnetized inflow model originate within a region of this size (Veledina et al. 2013). On the other hand, we clearly see a rise in IR flux as the source evolves through our hard state observations (see Figure 1). Therefore, under this same scenario, O-IR flux changes cannot be attributed solely to a change in the size of the hot inflow (see, e.g., Poutanen et al. 2014).

It is also relevant that in the hard state of GX 339-4 and other BHXRBs, the soft X-ray blackbody-like emission thought to originate from the geometrically thin, optically thick accretion disk is seen to vary significantly and also lead the correlated X-ray power-law variations, over the timescale range covered by the low- and high-frequency breaks observed here (Wilkinson & Uttley 2009; De Marco et al. 2015; De Marco et al. 2017). For geometrically thin disks, such relatively short (seconds) timescales of large-amplitude (tens of percent) disk continuum variability, presumably generated on the local viscous timescale, would be difficult to explain if the disk emission originates at $>100 R_G$, as would be implied by the hot-inflow model as presented in Veledina et al. (2013). On the other hand, on even shorter variability timescales (>1 Hz), blackbody "reverberation lags" are seen, some of which, if simply interpreted as light-travel times, could be consistent with such large radii (De Marco et al. 2017), but interpretation of such lags is complex, as their combination with the continuum lags is not simply additive (e.g., see Mastroserio et al. 2019 for the case of Fe K reverberation plus continuum lags in BHXRBs).
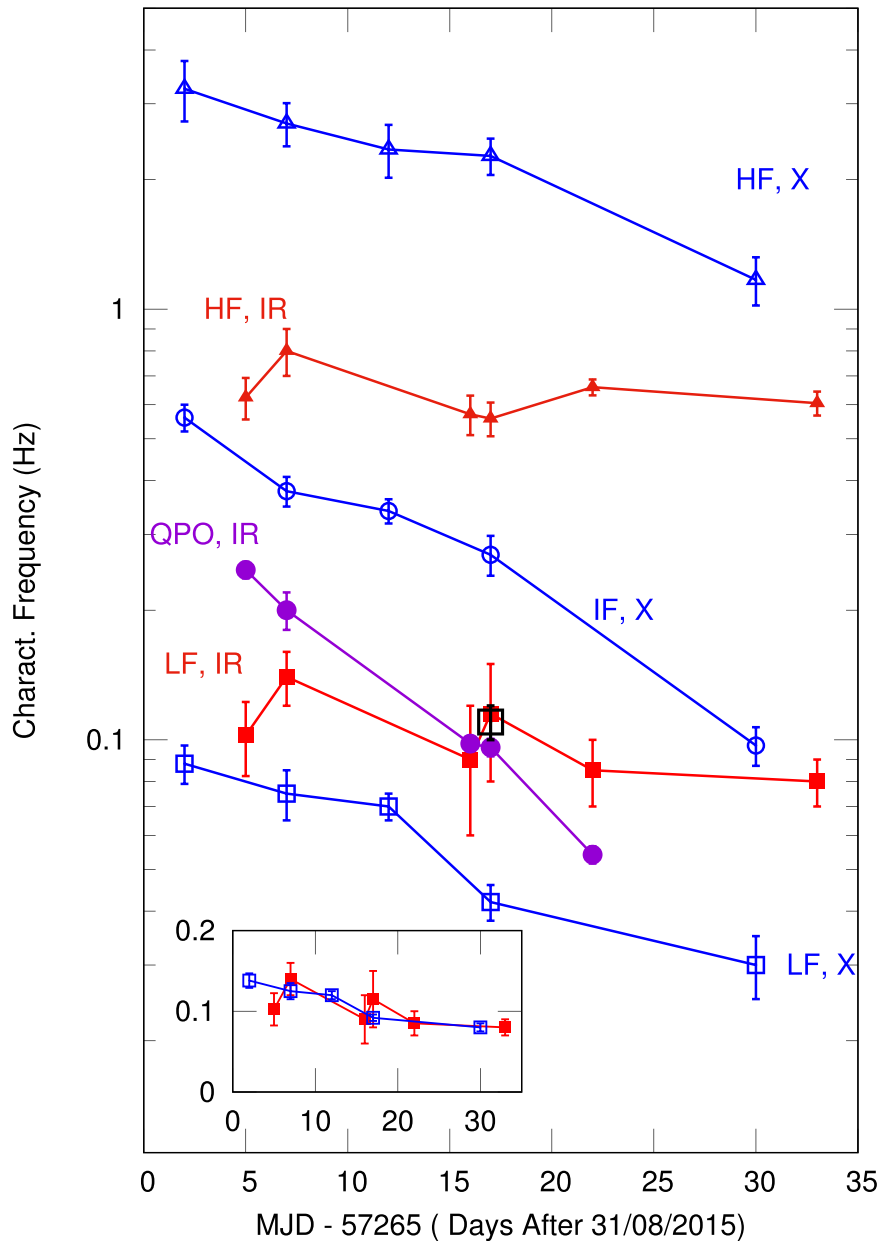
Figure 3. Evolution of the X-ray (blue) and IR (red) characteristic frequencies of the different Lorentzian components as a function of time. The low-frequency (LF) components are indicated with squares, while the high-frequency (HF) components with triangles. The intermediate-frequency X-ray component and the IR QPOs are indicated with circles, while the black square corresponds to the frequency of the marginally significant X-ray QPO. The inset shows a zoom on the two LF components in *linear* scale. We shifted $\nu_{X_{LF}}$ by +0.05 Hz, to show how the two frequencies are consistent with having a constant offset between each other.

Lags: The negative lags measured at low frequencies are naturally expected from the hot-inflow model (Veledina et al. 2011, 2017). On the other hand, the measured positive IR delay at high frequencies seems difficult to reconcile with this scenario, as it would imply that the Comptonized signal *leads* its seeds. We note that modeling of this scenario has been done only for a few observations during the intermediate state (Veledina et al. 2017; Veledina 2018). Therefore, new dedicated simulations are needed to test the model also in the hard state.

4.3. Compact Jet—Internal shocks

In this scenario, the whole IR variable emission is interpreted in terms of synchrotron emission from a jet, in which shells with different velocity collide and dissipate their differential

energy (Jamil et al. 2010; Malzac 2014; Malzac et al. 2018). The shell Lorentz factor PSD is assumed to be identical to the X-ray PSD, which is assumed to be a proxy for the accretion rate. Fast fluctuations in the shell speed will cause the shells to collide early in the jet, dissipating and then radiating away very soon their (differential) kinetic energy. Shorter- (longer-) wavelength emission, coming from inner (outer) regions in the jet, will present faster (slower) variability. At any given wavelength, the dissipation and radiation timescales in the shock sets an upper limit on the frequency of variability that can be observed, quenching faster variability (Malzac et al. 2018). Frequency damping depends on several physical parameters, including the average Lorentz factor, the jet inclination, the average accretion rate, and the properties of the injected variability. Thus, the observed stability of this

Table 1
Fits of Characteristic Frequencies Trends

Frequency versus Time Band	a_{LF} (10^{-2} Hz days^{-1})	b_{LF} (Hz)	a_{IF} (10^{-2} Hz days^{-1})	b_{IF} (Hz)	a_{HF} (10^{-2} Hz days^{-1})	b_{HF} (Hz)
IR	0.15 ± 0.1	0.08 ± 0.05	1.05 ± 0.09	0.2 ± 0.1	1.6 ± 4	0.4 ± 0.3
X-rays	0.21 ± 0.05	0.05 ± 0.04	1.39 ± 0.14	0.3 ± 0.2	7 ± 2	1.9 ± 1.4
Frequency versus Frequency Bands	a	b (Hz)				
$\nu_{X_{HF}}$ versus $\nu_{X_{LF}}$	32 ± 9	0.36 ± 0.44				
$\nu_{IR_{HF}}$ versus $\nu_{IR_{LF}}$	0 ± 2	0.6 ± 0.2				

Note. The top table reports the fit of three components as a function of time ($\nu = -a\,t + b$). Where t is time in days starting from MJD 57265. In the bottom one we show the results of the fit linking the evolution of different components within one single electromagnetic band. In particular we focused on the trend between the low- and the high-frequency component, i.e., $\nu_{HF} = a\,\nu_{LF} + b$. χ^2 test revealed that the fits were all acceptable within a 95% confidence interval. All errors are reported with a 90% significance level.

frequency during the outburst decay, while the X-ray flux and X-ray characteristic frequencies decay (Belloni et al. 2005; Dinçer et al. 2012; De Marco et al. 2017), provides strong quantitative constraints on this scenario.

Lags: The IR 0.1 s lag observed at high frequencies is easily explained in terms of travel time of the fluctuations from the inflow to the jet (Malzac 2014; Malzac et al. 2018). Malzac et al. (2018) have shown that also the negative lags observed at low frequencies can be accounted for by the model, due to a differential response of the shocks together with Doppler boosting modulation. Also in this case, dedicated simulations are in order to quantify this scenario for this data set.

4.4. Disk–Jet Connection—Launching Radius

Here we focus on the possibility that the observed IR variable emission originates in a jet, but that the quenching of the IR high-frequency variability happens at the jet-launching site, i.e., not all the variability in the inflow is transferred into the jet. This could happen if a Blandford & Payne (1982) launching mechanism is at play (as suggested by radio imaging of the jet in M87 and 3C84; Doeleman et al. 2012; Giovannini et al. 2018; see, however, Liska et al. 2018). In this case, the jet would tap matter (and accretion rate fluctuations) from a range of radii, between the innermost stable orbit and some radius R_{launch} (Spruit 2010). Assuming that each observed X-ray Fourier frequency is associated with the viscous timescale at a given radius (Done et al. 2007), and that variability originated at any radius propagates inward through the inflow (Uttley & McHardy 2001; Uttley et al. 2014), this implies that variability (much) faster than the viscous timescale at R_{launch} will contribute (much) less to the overall fluctuations transferred into the jet.

It is useful to recall here that the high-frequency component in the X-ray PSD shows a saturation at a few Hz in several BHXRBs (Churazov et al. 2001; Belloni et al. 2005; Ingram & Done 2012). Such a timescale is consistent with the viscous timescale at the last stable orbit (R_{ISCO}) of a hot inflow around a black hole of $\approx 10 M_\odot$. For GX 339–4, this (assumed) viscous frequency at R_{ISCO} is ≈ 2–5 Hz (Done et al. 2007), i.e., ≈ 4–10 times the value we measure for the high-frequency IR component. If the latter corresponds to the viscous frequency ν_{visc} at the launching radius, as $\nu_{visc} \propto R^{-3/2}$, it follows that the size of the launching region would be

$R_{launch} = (4$–$10)^{2/3} R_{ISCO}$, i.e., of the order of $\sim 10 R_G$. We caution the reader that this estimate is very rough, as it depends on many assumptions and on unknown parameters, such as the thickness and viscosity of the hot flow, and serves only as a figure of merit to test the scenario. We note that, in past outbursts from this source, the IR flux from GX 339–4 has been observed to drop by 3 mag in just a few days—as the source leaves the hard state—when the X-ray low-frequency component is at a frequency ≈ 0.55 Hz (Belloni et al. 2005; Homan & Belloni 2005). This frequency is very close to the high-frequency IR component we measure, which is consistent with a scenario in which the inferred inflow becomes comparable in size to the jet-launching region, causing the jet to quench.

Lags: Also in this case, the IR 0.1 s lag observed at high frequencies can be intuitively explained in terms of travel time of the fluctuations from the inflow to the jet. The low-frequency lags are instead more difficult to interpret, as this specific disk–jet scenario focuses on the high-frequency variability. Any prediction on the low-frequency behavior would be necessarily model dependent, and is beyond the scope of this work.

5. Conclusions

We have analyzed data from a quasi-simultaneous, multi-epoch X-ray/IR fast-photometry campaign of GX 339–4 during its 2015 outburst decay. We studied the evolution of the Fourier power density spectra in the two wavelengths. Our main result is the discovery of the stability of the characteristic frequencies of the IR variability, in particular of the high-frequency component, which is consistent with remaining constant at ~ 0.63 Hz throughout the campaign. We discuss possible physical interpretations of this result, and conclude that the most plausible explanation is in terms of variability from the X-ray-emitting inflow being transferred into an IR-emitting jet, although all models will need to be tested quantitatively against this result. Future multiwavelength campaigns, with multiple simultaneous bands in the optical–IR range, will help to disentangle between the scenarios.

ORCID iDs

F. M. Vincentelli ⓘ https://orcid.org/0000-0002-1481-1870
P. Casella ⓘ https://orcid.org/0000-0002-0752-3301
P. Petrucci ⓘ https://orcid.org/0000-0001-6061-3480
T. Maccarone ⓘ https://orcid.org/0000-0003-0976-4755
D. M. Russell ⓘ https://orcid.org/0000-0002-3500-631X
B. De Marco ⓘ https://orcid.org/0000-0003-2743-6632
P. Gandhi ⓘ https://orcid.org/0000-0003-3105-2615
J. Malzac ⓘ https://orcid.org/0000-0003-3334-3424
K. O'Brien ⓘ https://orcid.org/0000-0002-4744-3429
J. A. Tomsick ⓘ https://orcid.org/0000-0001-5506-9855

References

Belloni, T., & Hasinger, G. 1990, A&A, 227, L33
Belloni, T., Psaltis, D., & van der Klis, M. 2002, ApJ, 572, 392
Belloni, T., Homan, J., Casella, P., et al. 2005, A&A, 440, 207
Uttley, P., Wilkinson, T., Cassatella, P., et al. 2011, MNRAS, 414, L60
Blandford, R. D., & Payne, D. G. 1982, MNRAS, 199, 883
Casella, P., Belloni, T., & Stella, L. 2005, ApJ, 629, 403
Casella, P., Maccarone, T. J., O'Brien, K., et al. 2010, MNRAS, 404, L21
Churazov, E., Gilfanov, M., & Revnivtsev, M. 2001, MNRAS, 321, 759
Corbel, S., & Fender, R. P. 2002, ApJL, 573, L35
Corbel, S., Aussel, H., Broderick, J. W., et al. 2013, MNRAS, 431, L107
De Marco, B., Ponti, G., Muñoz-Darias, T., & Nandra, K. 2015, ApJ, 814, 50
De Marco, B., Ponti, G., Petrucci, P. O., et al. 2017, MNRAS, 471, 1475
Dhillon, V. S., Marsh, T. R., Stevenson, M. J., et al. 2007, MNRAS, 378, 825
Dinçer, T., Kalemci, E., Buxton, M. M., et al. 2012, ApJ, 753, 55
Doeleman, S. S., Fish, V. L., Schenck, D. E., et al. 2012, Sci, 338, 355
Done, C., Gierliński, M., & Kubota, A. 2007, A&ARv, 15, 1
Fender, R. P., Pooley, G. G., Durouchoux, P., Tilanus, R. P. J., & Brocksopp, C. 2000, MNRAS, 312, 853
Gandhi, P., Makishima, K., Durant, M., et al. 2008, MNRAS, 390, L29
Gandhi, P., Dhillon, V. S., Durant, M., et al. 2010, MNRAS, 407, 2166
Gandhi, P., Blain, A. W., Russell, D. M., et al. 2011, ApJL, 740, L13
Gandhi, P., Littlefair, S. P., Hardy, L. K., et al. 2016, MNRAS, 459, 554
Gandhi, P., Bachetti, M., Dhillon, V. S., et al. 2017, NatAs, 1, 859

Giovannini, G., Savolainen, T., Orienti, M., et al. 2018, NatAs, 2, 472
Homan, J., & Belloni, T. 2005, Ap&SS, 300, 107
Ingram, A., & Done, C. 2012, MNRAS, 419, 2369
Ingram, A., Done, C., & Fragile, P. C. 2009, MNRAS, 397, L101
Ingram, A., van der Klis, M., Middleton, M., et al. 2016, MNRAS, 461, 1967
Jamil, O., Fender, R. P., & Kaiser, C. R. 2010, MNRAS, 401, 394
Kalamkar, M., Casella, P., Uttley, P., et al. 2016, MNRAS, 460, 3284
Kalemci, E., Arabacı, M. Ö., Güver, T., et al. 2014, MNRAS, 445, 1288
Kara, E., Steiner, J. F., Fabian, A. C., et al. 2019, Natur, 565, 198
Kotov, O., Churazov, E., & Gilfanov, M. 2001, MNRAS, 327, 799
Liska, M., Hesp, C., Tchekhovskoy, A., et al. 2018, MNRAS, 474, L81
Mahmoud, R. D., Done, C., & De Marco, B. 2019, MNRAS, 486, 2137
Malzac, J. 2014, MNRAS, 443, 299
Malzac, J., & Belmont, R. 2009, MNRAS, 392, 570
Malzac, J., Kalamakar, M., Vincentelli, F., et al. 2018, MNRAS, 480, 2054
Markoff, S., Falcke, H., & Fender, R. 2001, A&A, 372, L25
Motch, C., Ilovaisky, S. A., & Chevalier, C. 1982, A&A, 109, L1
Motta, S., Belloni, T., & Homan, J. 2009, MNRAS, 400, 1603
Motta, S., Muñoz-Darias, T., Casella, P., Belloni, T., & Homan, J. 2011, MNRAS, 418, 2292
Narayan, R., & Yi, I. 1995, ApJ, 452, 710
Nowak, M. A., Vaughan, B. A., Wilms, J., Dove, J. B., & Begelman, M. C. 1999, ApJ, 510, 874
Pirard, J.-F., Kissler-Patig, M., Moorwood, A., et al. 2004, Proc. SPIE, 5492, 1763
Poutanen, J., & Vurm, I. 2009, ApJL, 690, L97
Poutanen, J., Veledina, A., & Revnivtsev, M. G. 2014, MNRAS, 445, 3987
Russell, T. D., Miller-Jones, J. C. A., Sivakoff, G. R., et al. 2016, MNRAS, 460, 3720
Spruit, H. C. 2010, LNP, 794, 233
Stiele, H., & Kong, A. K. H. 2017, ApJ, 844, 8
Strüder, L., Briel, U., Dennerl, K., et al. 2001, A&A, 365, L18
Thorne, K. S., & Price, R. H. 1975, ApJL, 195, L101
Uttley, P., & McHardy, I. M. 2001, MNRAS, 323, L26
Uttley, P., Cackett, E. M., Fabian, A. C., Kara, E., & Wilkins, D. R. 2014, A&ARv, 22, 72
Veledina, A. 2016, ApJ, 832, 181
Veledina, A. 2018, MNRAS, 481, 4236
Veledina, A., Poutanen, J., & Vurm, I. 2011, ApJL, 737, L17
Veledina, A., Poutanen, J., & Vurm, I. 2013, MNRAS, 430, 3196
Veledina, A., Gandhi, P., Hynes, R., et al. 2017, MNRAS, 470, 48
Vincentelli, F. M., Casella, P., Maccarone, T. J., et al. 2018, MNRAS, 477, 4524
Wang-Ji, J., García, J. A., Steiner, J. F., et al. 2018, ApJ, 855, 61
Wilkinson, T., & Uttley, P. 2009, MNRAS, 397, 666
Zdziarski, A. A., & Gierliński, M. 2004, PThPS, 155, 99